Rapid identification of neuronal structures in electronic microscope image using novel combined multi-scale image features

Jingwen Zhao, Hui Li, Meng Duan, Shuo Hong Wang, Yan Qiu Chen*

School of Computer Science, Shanghai Key Lab of Intelligent Information Processing, Fudan University, Shanghai 201203, China

ARTICLE INFO

ABSTRACT

This paper proposes an incremental scheme to identify the neurons in electronic microscope image. It first computes the probability of each pixel being cell membrane and then determines the image areas of the neurons. Our contributions also include novel combined multi-scale image features that are computationally efficient and provide strong discrimination ability for differentiating membrane pixels from other pixels. Experiment results show that the proposed system offers much higher speed than the compared state-of-the-art methods while produces comparably high accuracy.

1. Introduction

Identification of neuronal structures in electronic microscope(EM) image, i.e., to find the neurons and sub-cellular components, is key to 3D reconstructing neural circuits from EM image stacks [1,2], a research area drawing increasing international efforts due to its high value in assisting mankind's pursuit to understand how brains work [3,4]. One major benefit from such knowledge is the successful development of artificial neural networks.

On the road towards achieving the goal we face two challenges: (1) It is a difficult problem due to the vast variation of the shape and texture of neuron image and noise from the imaging process. Fig. 1 gives an example where vesicles, synapses and noises scatter erratically. (2) The image data is huge - a complete rat cortex of 500 mm^3 would produce about an exabyte(10^{18}) of data [5]. The identification algorithm must be computationally efficient to be practically useful [6].

After many years of intense research [7,8], steady progress has enabled the state-of-the-art systems to perform the task usefully. They are however far from being very satisfactory, and continued research is highly desirable.

The main limitations of the existing approaches are: (1) The identification accuracy is not sufficiently high and the resultant mistakes [9] in the reconstructed 3D neural circuits impede a thorough understanding of how a collection of neurons work to produce cognitive abilities; (2) The computational efficiency is inadequate [10] for 3D reconstructing the neural circuits of an entire cortex within a reasonable period of time.

To overcome the limitations of the current methods, we propose a novel two-step procedure that first uses combined multi-scale image features and random forest as classifier to obtain a probability map, and then uses improved watershed segmentation method to determine the image areas of the neurons. Our method extracts intrinsic features taking context information, intensity variation and shape cues into consideration, which significantly cuts down learning and classification time in classifying each pixel. The segmentation step obtains individual neurons to avoid mistakes in most supervised methods brought by discontinuities in imaged membranes.

The contributions of our work include:

- Proposing a novel incremental procedure, i.e., to compute a probability map first and then obtain the image areas of the neurons.
- Proposing two new features MSR and C2RB that provide strong discrimination information while being computationally inexpensive.
- Offering both high accuracy and high speed as demonstrated by experiment results.

2. Related work

Early in 1980s, researchers spent 10–15 years on completing the first connectome to describe the connectivity between all 302 neurons in the nematode worm Caenhorabditis elegans [11]. It took too long and too much manual work.

Thereafter, advances in electron microscope technology and better reconstruction algorithms change the situation and reconstruction work steps into a new stage [12].

---

* Corresponding author.
E-mail addresses: jingwenzhao13@fudan.edu.cn (J. Zhao), Hui_li@fudan.edu.cn (H. Li), mduan11@fudan.edu.cn (M. Duan), sh_wang@fudan.edu.cn (S.H. Wang), chenyq@fudan.edu.cn (Y.Q. Chen).
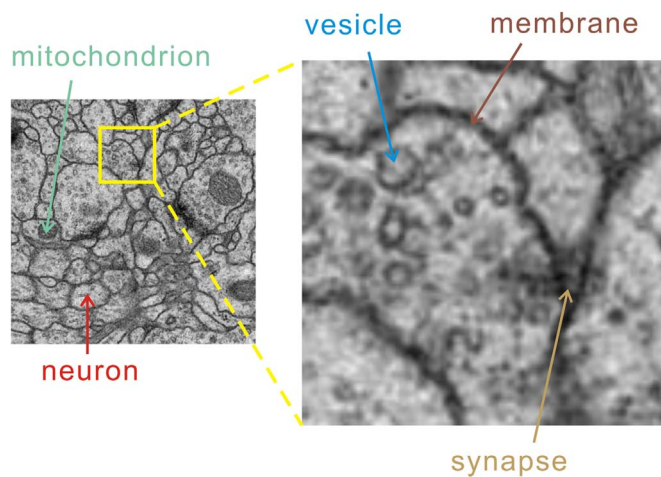
Fig. 1. An electronic microscope image of brain tissue.

Anisotropic directional filtering was applied to enhance membrane continuity [13] but lost segmentation with sufficient accuracy. Macke et al. [4] minimized an energy function for cell membranes but his active counter model failed due to mistakenly computed local minima in complex background and may find false boundaries. Nhat Vu and B.S. Manjunath [14] used graph cuts to minimize an energy defined over the image intensity and the flux of the intensity gradient field, it however required user interaction at first. All these unsupervised methods are defeated in accuracy by supervised ones since the latter train massive samples as priori knowledge.

Jurrus et al. [15] presented a framework to detect neuron membranes that integrates information from the original image together with contextual information by learning a series of artificial neural networks. Nevertheless this approach ignored geometric information of membranes and too many layers of classifiers make it far from a high speed. Seyedhosseini et al. [9] proposed to apply Radon-like features in his serial classifiers as geometric features specifically designed for connectome images apart from contextual information [10,16] etc used. However, result showed that Radon-like features only achieve modest accuracy levels. Ciresan et al. [10] applied deep neural networks for membrane detection and achieved excellent results, but it learned the filters for classification directly from data, and the multiple convolutions throughout the layers of the network accounted for an increasing filter support region. Above all, it consumed too much time. Other approaches such as [17,18] merely modified the probability map produced through their approaches but failed to solve problems at their source. Zhu F et.al [19] put forward an interesting reinforcement learning-based boundary amendment method after a multi-scale fused structure boundary detection algorithm, which achieved fairly good performance.

The supervised methods neglect intrinsic features possessed by membranes and are dependant on their classifiers which consume long time and demand a great deal of training examples. Meanwhile, membrane detection results outputted from these classifiers are discontinuous frequently. To overcome these limitations, we employ a correlation to rotational bar descriptor as our shape cues and compute intensity variation to implement contextual information to obtain suitable features. With the help of the proposed features classifiers are released from heavy computation for less processing time and finally we identify individual neurons surrounded by consecutive membranes using a segmentation strategy.

3. Proposed method

We adopt the 2D to 3D approach instead of directly reconstructing in 3D space due to the consideration of anisotropic nature of EM image stack, and the huge memory demand by the direct 3D reconstruction approach.

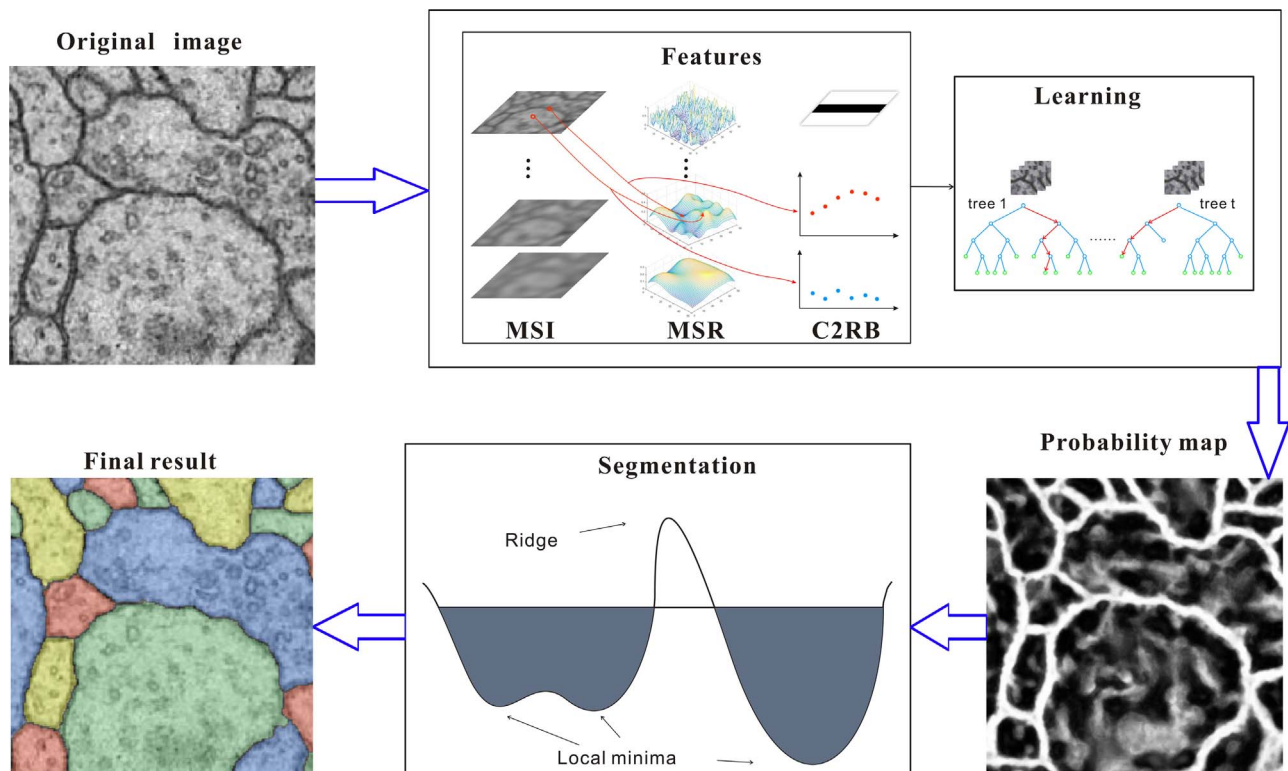The proposed method consists of three stages as illustrated in Fig. 2:

Fig. 2. Flow chart of the proposed method.

- Extracting features to characterize cell membranes.
- Learning to detect membrane pixels.
- Segmenting the image to obtain individual neurons.

3.1. Features

Good features should preserve the difference between distinct classes while reduce the variation within the same class. We observe that neuronal membranes appear as thin and elongated dark belts in electronic microscope images. They however do not appear as ideal dark belts on top of smooth brighter background. There is strong noise and other blob-like cellular components scattered around, which makes the task challenging.

We propose three types of descriptors reflecting the appearance characteristics of the membrane in order for the classifier to use the combination to achieve high accuracy: (A) Multi-scale intensity captures foreground and background context used alone by many researchers for membrane detection; (B) Multi-scale eigenvalue ratio describes variation of gray values in different direction; (C) Correlation of angles reflects shape peculiarity and differentiate rotational slender structures from others.

3.1.1. Multi-scale intensity (MSI)

To characterize darker membranes and brighter neighboring pixels at each pixel, we apply a series of Gaussian filters to the context image consecutively to generate a scale-space representation and obtain MSI for image I, which is widely used for its rich contextual information [9]:

$$MSI^\sigma(x, y) = (I*G^\sigma)(x, y) \tag{1}$$

where

$$G^\sigma(x, y) = \frac{1}{2\pi\sigma^2}e^{-\frac{x^2+y^2}{2\sigma^2}} \tag{2}$$

where * denotes the convolution operator, σ^2 is referred to as a scale parameter. As σ increases, the scale-space representation of the signal tends to coarser scales while a smaller one makes minutiae more apparent.

3.1.2. Multi-scale eigenvalue ratio (MSR)

In order to distinguish membrane from noise pixels that may appear as dark as the former, we utilize the observation that membranes stay at similar pixel values in a certain direction, but imaging noises and vesicles take variable values in all directions and scales, which leads to different ratios between the smaller eigenvalue and the larger one in a variation matrix of gray value(also termed *a* second moment matrix). The matrix is defined as:

$$M(x, y) = (g*\nabla I \nabla I^T)(x, y) \tag{3}$$

where $g(x, y)$ is a gaussian function for reducing effects of noise in remote area and

$$\nabla I(x, y)\nabla I^T(x, y) = \begin{pmatrix} I_x^2 & I_x I_y \\ I_x I_y & I_y^2 \end{pmatrix} \tag{4}$$

Two eigenvalues λ_1 and λ_2, that denote two directions in which curvature changes fastest in a local region, are corresponding for two orthogonal eigenvectors in a second moment matrix for measuring variation of gray values. Eigenvalue ratios for noise pixels vary from high to low among a neighborhood while those for membrane pixels stay at a low level as Fig. 3 illustrates. Harris [20] applied large eigenvalues to detect corners and achieved good results while we use the eigenvalues in a different way to distinguish membrane pixels from noise pixels. One characteristic is very clear shown in Fig. 3 that ratios of noise pixels change sharply but ratios of membrane pixels are similar. To describe stability and low ratio of membrane pixels other than that of noise pixels, we design another multi-scale descriptor,
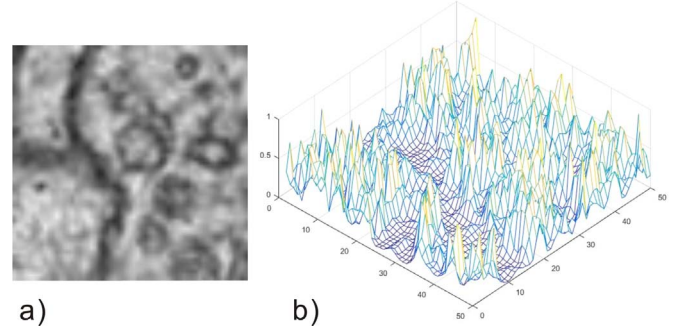

Fig. 3. Visualization of MSR feature. Gently undulating flat area in b) corresponds to membranes with low intensity while other steep mountains are ratios (MSR) generated by cytoplasm pixels mixed with weak (imaging) and strong (vesicle) noises. (a) EM image. (b) Visualization of MSR feature in 3D.

multi-scale eigenvalue ratio:

$$MSR^\sigma(x, y) = (\mathcal{R}*G^\sigma)(x, y) \tag{5}$$

where

$$\mathcal{R}(x, y) = \frac{\lambda_1(x, y)}{\lambda_2(x, y)} \tag{6}$$

where $G, *, \sigma$ are defined the same as what they are in MSI and λ_1 indicates the smaller eigenvalue while λ_2 is larger.

3.1.3. Correlation to rotational bar (C2RB)

Membranes resembling dark belts differ in shape from oval mitochondria, which can be described by a special Haar-like feature. The pliable sheet of tissue that lines organs or cells resembles a white and black and white square template H in original haar-like features. In consideration of quasi-circular membranes, a rotated version [21] of the black bar in Fig. 4 is employed to detect every corner of the elongated structures in all directions.

The traditional Haar-like feature [22] used in [23,24] are designed to measure the difference in intensity between two adjacent rectangular regions and can represent the local appearance of object. According to labels in ground truth provided by experts and large amounts of experiments, we set width of the black bar as w. Withal normalized cross correlation is a good criterion of similarity between two images, the correlation between template and a subimage at each pixel is applied as a shape descriptor. See its principle as follows:

$$C2RB^\theta(x, y) = \frac{1}{n}\sum_{x,y}\frac{(H_\theta(x, y) - \mu_{H_\theta})(J(x, y) - \mu_J)}{\sigma_{H_\theta}\sigma_J} \tag{7}$$

where n is the number of pixels in H_θ and the subimage J, μ is average and σ is standard deviation, θ indicates the rotated angle template H revolves. See [25] for more details on normalized cross correlation.
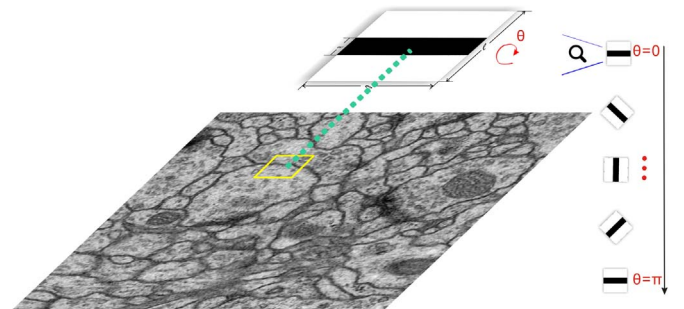

Fig. 4. Rotated square template in size $\ell \times \ell$ has a black rectangle whose width is w and length is the same as template. When template H is rotated from 0 to π, an array of correlation coefficients directly under every pixel are generated. A yellow rectangle illustrates an example at a pixel. (For interpretation of the references to color in this figure legend, the reader is referred to the web version of this article.)

After eight correlations are calculated at eight angles (illustrated in Fig. 4), we reorder correlations as a list of features according to their magnitude.

3.2. Classification via learning

Now that we have constructed features that contain discrimination information to tell whether a pixel is membrane, we need a classifier that can learn from annotated images to classify the pixels of new images. The problem is challenging as groups of vesicles and mitochondria clutter the background of EM images, making the pixel classification task very difficult.

We adopt random forests approach since its introduced randomness has increased the robustness to over-fitting and noise. Random forest classifier [26,27] is an ensemble of T decision trees, each consisting of split and leaf nodes. Each split node consists of a feature $f = \{MSI^\sigma, MSR^\sigma, C2RB^\theta\}$ and a threshold η. To classify pixel (x,y) in image I, one starts at the root and repeatedly evaluates f, branching left or right according to the comparison to threshold η.

Learning: For training of random forests, we use membrane pixels labeled by human experts in training set as positive and the rest as negative. And we find specifying the tree number as 300 can obtain effective and stable results. Each tree is trained on a different set of randomly synthesized images. A random subset of 2000 example pixels from each image is chosen to ensure a roughly even distribution. Each tree is trained using the following algorithm [28]:

- Choose multiple feature parameter w and threshold values η randomly for a set of split candidates: $\rho = (w, \eta)$.
- Partition the set of examples $\mathcal{L} = \{(x, y)\}$ into left and right subsets by each ρ.
- Compute ρ giving the largest gain in information.
- If the largest gain is sufficient, and the depth in the tree is below a maximum, then recurse for left and right subsets.

Classification: After trees are trained, every leaf node contains a probability, and for the n-th tree in class k, the probability is signed as $p_n(k)$. These probabilities for all trees can be combined to a forest's joint probability, just like a map(see Fig. 5(b)):

$$p(k) = \frac{1}{N} \sum_{n=1}^{N} p_n(k) \tag{8}$$

As we have only two classes, normalized probability indicating one pixel belongs to membrane class is saved as a value in a probability map P that is another intensity distributed image same as I.

3.3. Segmentation

The probability map obtained via the classification step indicates the likelihood of each pixel being membrane. In order to obtain the image area of each neuron, a segmentation process is needed. We adopt an improved watershed algorithm to achieve this goal. Using watershed algorithm after distance transformation has been proven feasible in biomedical image analysis [29], but there is no report of using it for determining the image areas of neurons.

In order to enhance membranes and eliminate vague area in a slightly low and similar intensity around membranes, distance transformation [30] transfer distances into intensities. Then the watershed algorithm [31] treats pixel intensities as ridge height. Regions with low intensity make an initial segmentation and with water level rising, small regions merge into large ones. Residual mitochondria boundaries and other light spots are easily flooded. Meanwhile, watershed algorithm aiming at closed regions fills gaps generated among membranes in the probability map.

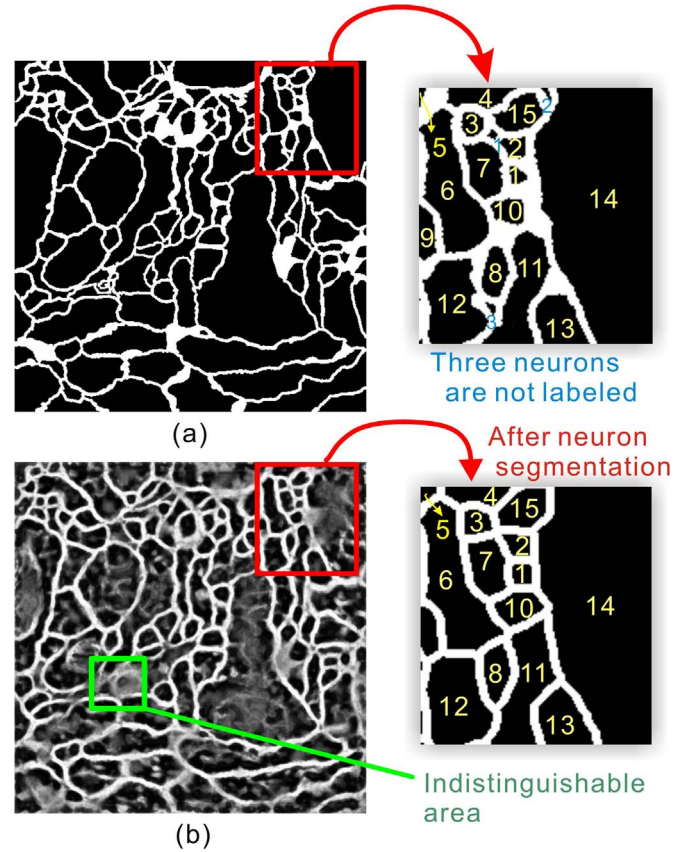Most methods threshold the probability map or use usual water-

Fig. 5. Results of the proposed method. Corresponding neuron sections are labeled the same number, while some parts are not assigned a number because probability map fails to recognize membranes and false mergers and splits appear. Green rectangle marks the most error-prone neurons that is distorted and possibly caused by an uneven cut during tissue slice preparation. (a) Ground truth. (b) Corresponding probability map. (For interpretation of the references to color in this figure legend, the reader is referred to the web version of this article.)

sheds but all these approaches can't work well for a good segmentation in the probability map since there are lots of missed gaps, noises or over-segmentation. Although as a simple approach, our method is efficient, effective and runs much faster than any learning step, such as [18].

We first define the improved watershed algorithm as:

$$c = \Phi(a, b) = h_1(h_2(a, b)) \tag{9}$$

where $h_2(.)$ denotes a distance transformation step and $h_1(.)$ indicates the watershed step.

Assume a label image after distance transformation is T, defined by pixels in the probability map P and a parameter τ which is related to S and U. Apparently, as for image I,

$$S = \Phi(P, \tau) \begin{cases} S = h_1(T) \\ T = h_2(P, \tau) \end{cases} \tag{10}$$

where $S = \{S_1, S_2, \ldots, S_m\}$ is the final segmentation of original image I and $U = \{U_1, U_2, \ldots, U_n\}$ is the ground truth image with the same size. Parameter m and n indicate how many neurons each image contains.

Except a traditional watershed step $h_1(.)$, details of $h_2(.)$ is as follows: Firstly we obtain Q as the background where $q \in Q$ is assigned 0 or 1 according to whether it is greater than τ. Then each pixel $t \in T$ equals to $\min_{q \in Q}(d(p, q))$ for each $p \in P$ at the same position where $d(a, b)$ is Euclidean distance $\sqrt{a^2 + b^2}$.

The optimal τ which aims at the optimal segmentation is obtained given the probability P and a gold standard segmentation U from train set with $\mathcal{A}$ images. This train set is one part included in our data set discussed in Section 4.

$$\tau = \underset{\tau \in [0,1]}{\mathrm{argmax}} \frac{\sum_{i \in [1,\mathcal{A}]} \sum_{k \in [1,n_i]} \max_{j \in [1,m_i]} |\Phi_j(P, \tau) \cap U_k|}{\sum_{i \in [1,\mathcal{A}]} |\bigcup_{k \in [1,n_i]} U_k|}$$

(11)

After Eq. (10) is performed, each successfully segmented neuron S_j is supposed to be assigned to one U_k as illustrated in Fig. 5 where all gaps of membranes in the probability map are closed:

$$S_j \sim U_k(k = \underset{k \in [1,n]}{\mathrm{argmax}} |S_j \cap U_k|)$$

(12)

4. Experiments

We performed experiments on two electronic microscope image stacks and compared the proposed method with state-of-the-art approaches.

4.1. Data sets

The first data set is a stack of 30 images with a resolution of 4×4×50 nm/pixel and 512×512 pixels from a serial section Transmission Electron Microscopy(ssTEM) data set of the Drosophila first instar larva ventral nerve cord (VNC) [32] with ground truth provided by the data set organizers. Although most of the image is clear enough for humans to recognize neurons, membranes and mitochondria, blurred area (circled red in Fig. 6 (a)) is messy dark and nothing could be distinguished even by human beings. Other vague membranes surrounded by slightly gray pixels also make the segmentation work hard.

The second data set is taken from calyx of drosophila brain (CAL) and captured by FEI Helios NanoLab 600i FIB-SEM. It consists of 100
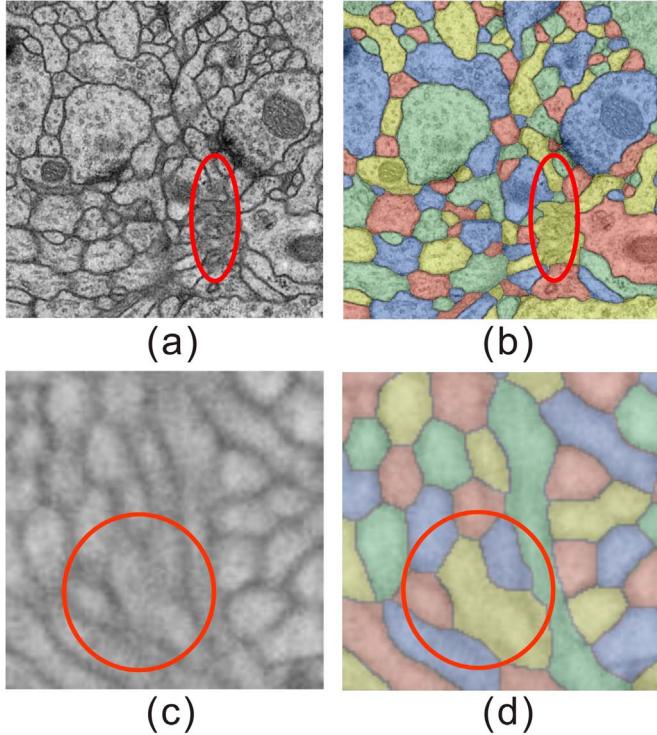

Fig. 6. Two samples in both data sets and their final segmentation map. Adjacent neurons in segmentation map is colored with different tint as to be distinct from each other. There are some indistinguishable neurons circled red in (a) and (c), and their corresponding results make a decision at those degraded areas. (a) Original image in VNC dataset. (b) Result image in VNC dataset. (c) Original image in CAL dataset. (d) Result image in CAL dataset. (For interpretation of the references to color in this figure legend, the reader is referred to the web version of this article.)

images with a resolution of 4096×4096 pixels corresponding to a 20×20×4 μm^3 section. CAL data set is from Aike Guo research group of *Shanghai Institutes for Biological Science* (Fig. 6 (c)(d)). The membranes appear less clear in this data set which increases the challenge to the algorithms. As it does not include ground truth, it is not used for comparison.

4.2. Performance metrics

4.2.1. Rand error

A widely used performance metric to evaluate the performance of image segmentation task where the goal is to detect boundary is precision-recall. Traditional one-to-one match between each pixel in a test segmentation and ground truth is however irrelevant as small changes in boundary detection can result in large topological differences between segmentations. Therefore, we use the Rand index metric which measures the resemblance of two clusters of segmentations and is regarded as a leading index in a publicly known challenge. The Rand index is based on the pairwise pixel metric introduced by Rand [33]. As for $S = \{S_1, S_2, ..., S_m\}$ and $U = \{U_1, U_2, ..., U_n\}$, true positives(TP), true negatives(TN), false positives(FP) corresponding to under-segmented pixel pairs and false negatives(FN) corresponding to over-segmented ones in Rand index are computed as:

$$TP = \sum_i \sum_{j>i} \lambda(s_i = s_j \wedge u_i = u_j)$$

(13)

$$TN = \sum_i \sum_{j>i} \lambda(s_i \neq s_j \wedge u_i \neq u_j)$$

(14)

$$FP = \sum_i \sum_{j>i} \lambda(s_i = s_j \wedge u_i \neq u_j)$$

(15)

$$FN = \sum_i \sum_{j>i} \lambda(s_i \neq s_j \wedge u_i = u_j)$$

(16)

where $\lambda(.)$ is a function that outputs 1 and 0 according to if the argument is true. $s_i \in S$ is assigned the same integer label that is unique for each object. So is u_i. Each calculation compares the labels of a given pixel pair (s_i, s_j) with its corresponding pixel pair (u_i, u_j). The F-score of Rand index is computed from these results using precision and recall where:

$$Precision = \frac{TP}{TP + FP}$$

(17)

$$Recall = \frac{TP}{TP + FN}$$

(18)

$$F - score = \frac{2 \times Precision \times Recall}{Precision + Recall}$$

(19)

Then rand error is obtained:

$$Rand\ error = 1 - F - score$$

(20)

4.2.2. Warping error

In addition to rand error, sometimes warping error [34] is also applied. Assume a binary image L is termed a boundary labeling of an image I, if a '0' pixel in L indicates the presence of a boundary between two objects in the image, and a '1' pixel indicates the presence of an object. Then we can obtain scores using this metric.

Warping error is a segmentation metric that penalizes topological disagreements, in this case, the object splits and mergers. Assume L^W is a warping of L, or $L^W \lhd L$ (detailed in [34]), then warping error between result labeling L^R and ground truth labeling L is the squared Euclidean distance between L and the "best warping" of L onto L^R:

$$Warping\ error = \min_{L^W \lhd L} \| L^R - L^W \|^2$$

(21)

Table 1
Accuracy and speed in different methods.

Method	Ncut	MSANN	MCMS	DNN	ECT	Prop
Rand error	0.393	0.151	0.089	**0.051**	0.082	**0.054**
Warping error(%)	2.51	3.09	0.11	**0.04**	0.23	0.15
Computation time(s)	401.46	50.02	52.25	203.45	8.15	**7.17**

Table 2
Accuracy in different features.

Feature	no C2RB	no MSI	no MSR
Rand error	0.071	0.191	0.185

4.3. Evaluation and discussions

We evaluate the proposed method on five different segmentation tasks in EM images, then the explanation is performed to find out the significance of each features proposed in Section 3.1 and the segmentation step in Section 3.3.

4.3.1. Comparisons with existing methods

Four state-of-the-art supervised methods and a well-known method without a classifier are chosen to compare performances including accuracy and processing speed. Due to the absence of the ground truth data for the testing set used in the ISBI 2012 EM Challenge, we performed a three-fold cross validation experiment by dividing VNC training set into three substacks. One stack with 250,000 pixels selected randomly are used for training and the other two was tested each time. The following comparisons with other methods are based on VNC data set.

The four supervised methods includes: (1) MSANN [9] which takes advantage of information from a larger area and improves the overall result of serial ANNs through exploiting multi-scale context for segmentation; (2) DNN [10] which applies a deep learning net work and achieves a leading result in 2012 ISBI Electron Microscopy Image Segmentation Challenge; (3) MCMS [35] which exploits contextual information from multiple objects and at different scales for learning discriminative models; (4) ECT [36] which aims to minimize false merges in segmentation. The chosen unsupervised method is an image segmentation approach termed Normalized Cut(Ncut) [37].

We test these five approaches on electron microscopy slices of VNC and list their scores of two widely used metrics in Table 1. Also, a computation time (spent by one image) contrast is shown. Supervised approaches are listed with their testing time because training is just a small part of reconstruction in which detecting membranes are the issue of crucial importance. Among these tables, our method is expressed as "Prop", and best results are labeled in bold.

The proposed method achieves the highest speed (less than 8 s) when processing each image. Benefited from the proposed features, MSR and C2RB, classifiers are released from heavy computation for less processing time. Firstly, testing an image for segmentation is apparently convenient and quick when one employ a trained classifier with a small number of features. Besides, the proposed features make classification rapid in account of feature's being extracted efficiently.

Conversely, MSANN and MCMS use too many layers of classifiers which makes them far from a high speed. DNN gives a poorer performance in computation time considering that it learned the filters for classification directly from data using deep neural networks, and the multiple convolutions throughout the layers of the network accounted for an increasing filter support region. Concerning ECT, although the test procedure cost less time, retraining is required for the supervised algorithm at each iteration, which can be time consuming especially when more iterations with fewer samples per iteration are used to maximize the utilization of supervised information and minimize human effort; Moreover, repeated human interactions may lead to extra cost overhead in practice. The unsupervised Ncut formulate the image segmentation problem as a graph partitioning problem which leads to $O(n^3)$ time for solving a standard eigenvalue
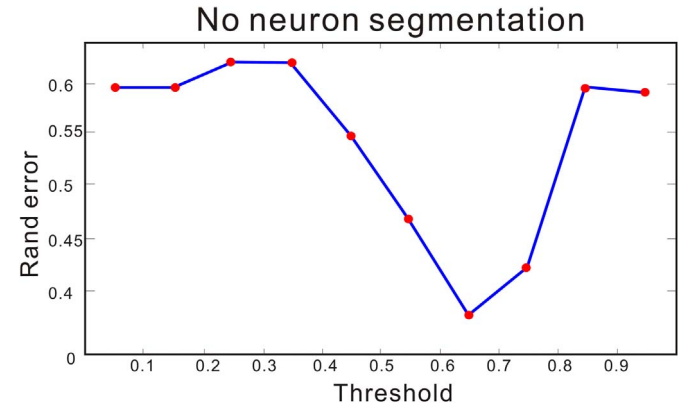

Fig. 7. Fscore without a segmentation step are illustrated in different thresholds.

problem for all eigenvectors where n is the number of pixels in the image.

The proposed method also achieves almost the same accuracy, 0.054 in rand error, as that of DNN that achieves a leading accuracy through scarifying a long time (more than 200 s). The lost accuracy of MSANN and MCMS is ascribed to the ignored geometric information of membranes. ECT does not directly explore the unsupervised information while searching for the optimal classification function. Ncut, as an unsupervised method, is defeated in accuracy by supervised ones since it lost priori knowledge compared with supervised ones.

Nevertheless, we must admit that our method lost out to MCMS and DNN in warping error as Table 1 shows for the sake of a less amount of computation. Certain essential information concerning membranes is missed when extracting features, which results in false mergers and splits and increases warping error since this error is designed to penalize false merges and splits.

Concerning the data set on CAL, it is more difficult for automatic detection on computers. The proposed method, however, detects most neurons, some of which even a man can hardly recognize. Neuron segmentation result of CAL is shown in Fig. 6.

4.3.2. The role of each step

To verify which feature is more effective towards the segmentation task, we performed several experiments by taking each feature out and the results is shown in Table 2. Here we just compare rand error, a leading index which measures similarity between two clusters or segmentations and is enough to rank the significance of features. The results in those experiments demonstrate MSI and MSR devote almost the same contribution, and perform better than C2RB does.

The significance of the segmentation step is evaluated by thresholding the probability map produced from the classifier at different levels as shown in Fig. 7. Experiments demonstrate the segmentation step significantly improves accuracy.

5. Conclusions

We have developed an efficient and effective neuronal structure identification algorithm. The main idea of our method is to take advantages of combined features, thereby providing the classifier with a richer set of discrimination information. We also apply an improved

watershed algorithm to cluster pixels assigned different probabilities into clustered regions called neurons. Results indicate that the proposed method outperforms state-of-the-art algorithms significantly in speed.

Acknowledgements

References

[1] D.B. Chklovskii, S. Vitaladevuni, L.K. Scheffer, Semi-automated reconstruction of neural circuits using electron microscopy, Curr. Opin. Neurobiol. 20 (5) (2010) 667–675.

[2] R. Kumar, A. Vázquez-Reina, H. Pfister, Radon-like features and their application to connectomics, in: Proceedings of the IEEE Conference on Computer Vision and Pattern Recognition Workshops (CVPRW), Computer Society , 2010, pp. 186–193.

[3] M. Helmstaedter, K.L. Briggman, W. Denk, High-accuracy neurite reconstruction for high-throughput neuroanatomy, Nat. Neurosci. 14 (8) (2011) 1081–1088.

[4] J.H. Macke, N. Maack, R. Gupta, W. Denk, B. Schölkopf, A. Borst, Contour-propagation algorithms for semi-automated reconstruction of neural processes, J. Neurosci. Methods 167 (2) (2008) 349–357.

[5] J.W. Lichtman, H. Pfister, N. Shavit, The big data challenges of connectomics, Nat. Neurosci. 17 (11) (2014) 1448–1454.

[6] V. Kaynig, A. Vazquez-Reina, S. Knowles-Barley, M. Roberts, T.R. Jones, N. Kasthuri, E. Miller, J. Lichtman, H. Pfister, Large-scale automatic reconstruction of neuronal processes from electron microscopy images, arXiv:1303.7186

[7] C. Jones, T. Liu, N.W. Cohan, M. Ellisman, T. Tasdizen, Efficient semi-automatic 3d segmentation for neuron tracing in electron microscopy images, J. Neurosci. Methods 246 (2015) 13–21.

[8] V. Kaynig, T. Fuchs, J.M. Buhmann, Neuron geometry extraction by perceptual grouping in sstem images, in: Proceedings of the IEEE Conference on Computer Vision and Pattern Recognition (CVPR), 2010, pp. 2902–2909.

[9] M. Seyedhosseini, R. Kumar, E. Jurrus, R. Giuly, M. Ellisman, H. Pfister, T. Tasdizen, Detection of neuron membranes in electron microscopy images using multi-scale context and radon-like features, in: Medical Image Computing and Computer-Assisted Intervention–MICCAI 2011, Springer, 2011, pp. 670–677.

[10] D. Ciresan, A. Giusti, L.M. Gambardella, J. Schmidhuber, Deep neural networks segment neuronal membranes in electron microscopy images, in: Advances in neural information processing systems, 2012, pp. 2843–2851.

[11] J. White, E. Southgate, J. Thomson, S. Brenner, The structure of the nervous system of the nematode Caenorhabditis elegans the mind of a worm, Philos. Trans. R. Soc. Lond. 314 (1986) 1–340.

[12] K.L. Briggman, W. Denk, Towards neural circuit reconstruction with volume electron microscopy techniques, Curr. Opin. Neurobiol. 16 (5) (2006) 562–570.

[13] T. Tasdizen, R. Whitaker, R. Marc, B. Jones, Enhancement of cell boundaries in transmission electron microscopy images, in: Proceedings of the IEEE International Conference on Image Processing, 2005. ICIP 2005, vol. 2, 2005, pp. II–129.

[14] N. Vu, B. Manjunath, Graph cut segmentation of neuronal structures from transmission electron micrographs, in: Image Processing, 2008. ICIP 2008. in: Proceedings of the 15th IEEE International Conference, 2008, pp. 725–728.

[15] E. Jurrus, A.R. Paiva, S. Watanabe, J.R. Anderson, B.W. Jones, R.T. Whitaker, E.M. Jorgensen, R.E. Marc, T. Tasdizen, Detection of neuron membranes in electron microscopy images using a serial neural network architecture, Med. Image Anal. 14 (6) (2010) 770–783.

[16] V. Jain, J.F. Murray, F. Roth, S. Turaga, V. Zhigulin, K.L. Briggman, M.N. Helmstaedter, W. Denk, H.S. Seung, Supervised learning of image restoration with convolutional networks, in: Computer Vision, 2007. ICCV 2007. IEEE in: Proceedings of the 11th International Conference on IEEE, 2007, pp. 1–8.

[17] C. Jones, M. Sayedhosseini, M. Ellisman, T. Tasdizen, Neuron segmentation in electron microscopy images using partial differential equations, in: Biomedical Imaging (ISBI), 2013 IEEE Proceedings of the 10th International Symposium on, IEEE, 2013, pp. 1457–1460.

[18] T. Liu, E. Jurrus, M. Seyedhosseini, M. Ellisman, T. Tasdizen, Watershed merge tree classification for electron microscopy image segmentation, in: Pattern Recognition (ICPR), 2012 Proceedings of the 21st International Conference on, IEEE, 2012, pp. 133–137.

[19] F. Zhu, Q. Liu, Y. Fu, B. Shen, Segmentation of neuronal structures using sarsa (λ)-based boundary amendment with reinforced gradient-descent curve shape fitting, PloS One 9 (3) (2014) e90873.

[20] C. Harris, M. Stephens, A combined corner and edge detector., in: Proceedings of the Alvey Vision Conference, vol. 15, Manchester, UK, 1988, p. 50.

[21] C. Messom, A. Barczak, Fast and efficient rotated haar-like features using rotated integral images, in: Proceedings of the Australian Conference on Robotics and Automation, 2006, pp. 1–6.

[22] D.-S. Chen, Z.-K. Liu, Generalized haar-like features for fast face detection, in: Proceedings of the Machine Learning and Cybernetics International Conference on IEEE, vol. 4, 2007, pp. 2131–2135.

[23] P. Viola, M. Jones, Rapid object detection using a boosted cascade of simple features, in: Computer Vision and Pattern Recognition, 2001. CVPR 2001.

[24] P. Viola, M. Jones, Robust real-time object detection, Int. J. Comput. Vis. 4 (2001) 34–47.

[25] J. Lewis, Fast normalized cross-correlation, in: Vision interface, vol. 10, 1995, pp. 120–123.

[26] Y. Amit, D. Geman, Shape quantization and recognition with randomized trees, Neural Comput. 9 (7) (1997) 1545–1588.

[27] L. Breiman, Random forests, Mach. Learn. 45 (1) (2001) 5–32.

[28] J. Shotton, T. Sharp, A. Kipman, A. Fitzgibbon, M. Finocchio, A. Blake, M. Cook, R. Moore, Real-time human pose recognition in parts from single depth images, Commun. ACM 56 (1) (2013) 116–124.

[29] G. Lin, U. Adiga, K. Olson, J.F. Guzowski, C.A. Barnes, B. Roysam, A hybrid 3d watershed algorithm incorporating gradient cues and object models for automatic segmentation of nuclei in confocal image stacks, Cytom. Part A 56 (1) (2003) 23–36.

[30] G. Borgefors, Distance transformations in digital images, Comput. Vis. Graph. Image Process. 34 (3) (1986) 344–371.

[31] F. Meyer, Topographic distance and watershed lines, Signal Process. 38 (1) (1994) 113–125.

[32] A. Cardona, S. Saalfeld, S. Preibisch, B. Schmid, A. Cheng, J. Pulokas, P. Tomancak, V. Hartenstein, An integrated micro-and macroarchitectural analysis of the drosophila brain by computer-assisted serial section electron microscopy, PLoS Biol. 8 (10) (2010) e1000502.

[33] W.M. Rand, Objective criteria for the evaluation of clustering methods, J. Am. Stat. Assoc. 66 (336) (1971) 846–850.

[34] V. Jain, B. Bollmann, M. Richardson, D.R. Berger, M. N. Helmstaedter, K.L. Briggman, W. Denk, J.B. Bowden, J.M. Mendenhall, W.C. Abraham, et al., Boundary learning by optimization with topological constraints, in: Proceedings of the IEEE Conference on Computer Vision and Pattern Recognition (CVPR), 2010, pp. 2488–2495.

[35] M. Seyedhosseini, T. Tasdizen, Multi-class multi-scale series contextual model for image segmentation, IEEE Trans. Image Process. 22 (11) (2013) 4486–4496.

[36] T. Parag, D.C. Ciresan, A. Giusti, Efficient classifier training to minimize false merges in electron microscopy segmentation, in: Proceedings of the IEEE International Conference on Computer Vision, 2015, pp. 657–665.

[37] J. Shi, J. Malik, Normalized cuts and image segmentation, IEEE Trans. Pattern Anal. Mach. Intell. 22 (8) (2000) 888–905.

Proceedings of the 2001 IEEE Computer Society Conference on, vol. 1, IEEE, 2001, pp. I–511.
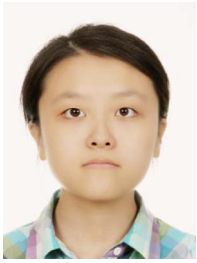
Jingwen Zhao received her BEng degree from East China University of Science and Technology in 2013. She is now pursuing her Ph.D. degree in School of Computer Science, Fudan University. Her current research interests include biological image processing, medical image analysis and pattern recognition.

Hui Li received his BEng degree from Shanghai University in 2011 and MEng degree from Fudan University in 2014. He is now a senior data analyst at Alipay and Alibaba Group.

Meng Duan received her BEng degree from Fudan University in 2016. She is now a research assistant in Brain Chip Research Center of Fudan University. Her current research interests include deep learning, biological image processing and pattern recognition.

Shuo Hong Wang received her BEng degree from East China University of Science and Technology in 2012. She is now pursuing her Ph.D. degree in School of Computer Science, Fudan University. Her research interests include multiple object tracking, biological and medical image analysis.

Yan Qiu Chen received his Ph.D. degree from Southampton University, United Kingdom in 1995, and his MEng and BEng degrees from Tongji University, Shanghai, China in 1988 and 1985 respectively.

Dr. Chen is currently a full professor and director of Computer Vision Lab with School of Computer Science of Fudan University, Shanghai, China,. He had been Chairman of Department of Communication Science and Engineering from 2004 through 2007, and Associate Chairman of Department of Computer Science and Engineering from 2002 through 2004. Dr. Chen was an assistant professor with School of Electrical and Electronic Engineering of Nanyang Technological University, Singapore from 1996 through 2001, and was a postdoctoral research fellow with Glamorgan University, UK in 1995.